Anion-Participating Solvation in Multi-Salt Cooperative Electrolytes for Enhanced Low-Temperature Li-storage capability

Bin Zhang[a], Qing Yin[a,] *, Shouxun Peng[a], Zeyu Zhao[a], Meiyu Shi[a], Xiwen Li[a], Zheng Li[a], Bin Xiao[a], Xiuquan Gu[a], Mingjia Zhi,[b] Eugene Chubenko,[c] Vitaly Bondarenko[c], Hanna Bandarenka[c] and Yanwei Sui[a,] *

a: School of Materials Science and Physics
China University of Mining and Technology
Xuzhou 221116, P. R. China

b: School of Materials Science and Engineering
Zhejiang University
866 Yuhangtang Road, Hangzhou, China

c: Belarusian State University of Informatics and Radioelectronics
P. Browka Str. 6, Minsk, 220013, Belarus

Corresponding authors:
E-mail: qingyin0715@cumt.edu.cn (Qing Yin); suiyanwei@cumt.edu.cn (Yanwei Sui)

Keywords: Low-temperature capability, Multi-salt electrolyte, Anion-participating solvation, Lithium-ion transport kinetics

Abstract: Low-temperature operation remains a major challenge because sluggish Li^+ transport and aggravated polarization severely compromise energy delivery and cyclability. Here we develop a wide-temperature tri-salt electrolyte comprising $LiBF_4$, LiFSI and LiDFOB in a PC/DME/iBA solvent matrix. With an optimized formulation (0.75 M $LiBF_4$, 0.2 M LiFSI, 0.05 M LiDFOB, PC : DME : iBA = 25:65:10, v/v/v , T-electrolyte), Li||$LiCoO_2$ batteries deliver high reversibility, strong rate capability and durable cycling from –20 to 40ºC. Remarkably, at –20°C, the optimized electrolyte sustains 143.5 mAh g^{-1} at 0.2 C and preserves 129.7 mAh g^{-1} after 500 cycles, corresponding to ~85.5% of the room-temperature capacity, whereas a conventional low-temperature electrolyte rapidly decays to 47.2 mAh g^{-1} over the same cycles. Raman spectroscopy and molecular dynamics (MD) simulations reveal that anions and iBA participation reconstruct the Li^+ solvation sheath by suppressing PC over-coordination and lowering representative cluster binding energies, thereby reducing the desolvation penalty and promoting anion-derived inorganic-enriched interphases. XPS reveals that the T-electrolyte stabilizes both Solid Electrolyte Interphase (SEI) and Cathode Electrolyte Interphase (CEI) by promoting LiF/$LiSO_xF$/borate-rich inorganic passivation while suppressing uncontrolled carbonate/ether decomposition, and by forming a self-limited cathode CEI in which $ROCO_2Li$ semicarbonates act as a compliant scaffold to preserve interfacial integrity under cycling at –20ºC. This work establishes a practical solvation-interphase design strategy for enhanced Li-storage at low temperature.

1. Introduction

As global energy systems transition toward renewable electricity generation and widespread transportation electrification, lithium-ion batteries (LIBs) or lithium metal batteries (LMBs) have become a cornerstone of modern and future energy infrastructure.[1] However, with the continuous expansion of application scenarios, they are increasingly expected to operate reliably not only near room temperature but

also under harsh thermal conditions, from extreme cold to moderately elevated temperatures and under rapidly fluctuating environments.[2, 3] Such all-climate operability is indispensable for electric vehicles in cold regions, unmanned aerial vehicles, grid-scale energy storage in harsh climate and aerospace systems. Under low-temperature conditions, however, battery performance is often governed more by electrolyte transport and interfacial processes than by the intrinsic capabilities of the electrode materials, because the sharp increase in viscosity, sluggish Li^+ desolvation and charge-transfer kinetics.[4–6] Therefore, developing electrolytes that deliver satisfactory capacity output and durable long-term cycling stability across a broad temperature window has become a critical challenge in advanced battery research.[7, 8] Despite the remarkable success of commercial LIBs, their electrochemical performance still relies predominantly on conventional $LiPF_6$-based carbonate electrolytes, typically composed of EC/DEC, EC/EMC and PC/DME, which exhibit inherent limitations under both sub-ambient and elevated temperatures, especially in terms of viscosity increase, sluggish Li^+ desolvation and unstable interphase formation.[9–12]

At low temperatures, numerous studies have demonstrated that high-dielectric carbonate solvents such as EC and PC strongly coordinate with Li^+ through their carbonyl oxygen atoms, giving rise to rigid solvation structures that impede Li^+ desolvation, increase viscosity and suppress ionic conductivity by one to two orders of magnitude. These results indicate that low-temperature electrolyte design should consider not only bulk transport properties, but also local Li^+ coordination and ion-speciation regulation.[13, 14] Thenuwara et al. further revealed that low temperatures significantly slow solvent reduction kinetics, leading to incomplete decomposition of EC and DMC and the accumulation of organic species in the solid electrolyte interphase (SEI), while simultaneously suppressing $LiPF_6$ decomposition, thereby decreasing the LiF content and mechanical robustness of the SEI.[15] In addition, PC undergoes more intensive reductive decomposition at low temperatures, generating large amounts of

carbonates species and forming thick, resistive, and chemically unstable SEI layers that severely compromise low-temperature cycling performance.[16] At elevated temperatures, however, the intrinsic ithermal and hydrolytic instability of $LiPF_6$ becomes a primary source of battery degradation.[17] Chen et al. demonstrated that the labile P−F bond in $LiPF_6$ readily dissociate, generating PF_5, POF_3 and HF, which aggressively attack the cathode surface, promote transition-metal dissolution and destroy both the SEI and cathode electrolyte interphase (CEI).[18] Similarly, Choi et al. confirmed that $LiPF_6$ undergoes hydrolysis to produce HF together with protic species (ROH/H_2O), which further decompose the carbonate solvent matrix and continuously corrode interfacial films.[19] These degradation pathways are particularly detrimental for Si-based anodes, where HF reacts with the native SiO_2 layer to form unstable SiO_xF_y species, exacerbating interfacial instability and capacity fading. Consequently, conventional $LiPF_6$-based single-salt carbonate electrolytes are intrinsically ill-suited for truly wide-temperature operation, especially under prolonged low-temperature cycling and storage.

To enhance temperature resilience, intensive efforts have been devoted to electrolyte engineering by tuning lithium salt chemistry, solvent matrices and interfacial regulation strategies.[20] Representative approaches include optimized $LiPF_6$/EC-PC-EMC mixtures,[21] LiTFSI-containing binary or ternary salt blends,[22] EC/DMC/DEC carbonate formulations,[23] partially fluorinated ester-based gel electrolytes[24] and dual-salt $LiPF_6$-LiFSI systems[25]. These studies suggest that effective low-temperature electrolytes require a balanced combination of low viscosity, sufficient salt dissociation, weakened Li^+ solvation and stable SEI/CEI-forming chemistry, and these designs can improve bulk ionic conductivity or cold-temperature discharge performance, yet they still suffer from insufficient capacity retention or limited low-temperature reversibility over extended cycling. Given these limitations, $LiBF_4$ has attracted growing attention as an alternative lithium salt owing to its higher

thermal stability, phosphorus-free composition, suppressed HF generation compared to $LiPF_6$, and relatively modest viscosity increase at low temperatures.[26, 27] However, $LiBF_4$ alone is hampered by limited solubility, relatively weak ionic dissociation and poor passivating film-forming ability in many organic solvents, which together result in unsatisfactory long-term cycling stability. To overcome these drawbacks, lithium difluoro(oxalato)borate (LiDFOB) has been extensively investigated as a multifunctional salt and interfacial film-forming additive. Upon electrochemical decomposition, LiDFOB generates $B{-}O^-$, $B{-}F^-$ and LiF-rich inorganic species that build mechanically robust and chemically stable interphases, which in turn markedly improves long-term cycling and rate capability.[28–30] Beyond salt chemistry, solvent engineering further expands the electrolyte design space.[31, 32] Weakly solvating electrolytes (WSEs) have emerged as an effective strategy to lower Li^+ desolvation energy barriers and promote the formation of inorganic-rich, mechanically robust SEI formation.[33] Conventional carbonates such as PC and EC provide strong solvation power but suffer from sluggish low-temperature kinetics, whereas ethers such as DME afford high Li^+ diffusivity but exhibit limited reductive stability on low-potential anodes.[34] Thus, introducing weakly coordinating, low-viscosity esters such as iso-butyl acetate (iBA) can effectively tailor the primary solvation shell, suppresses excessive PC coordination, and improves low-temperature Li^+ desolvation kinetics.[35] When combined with FSI^- or $DFOB^-$ anions, such ester-containing formulations further enhance the thermal and oxidative stability of the electrolyte.

Motivated by these insights, we propose a $LiBF_4$/LiFSI/LiDFOB tri-salt electrolyte (hereafter denoted as T-electrolyte) paired with a PC/DME/iBA ternary solvent system for long-term cycling Li||$LiCoO_2$ batteries from −20ºC to 40ºC. This formulation is rationally designed to weaken excessive carbonyl coordination, introduce multi-anion participation in the Li^+ solvation sheath, and reduce electrolyte viscosity, As a result, it facilitates inorganic-rich, mechanically robust SEI/CEI

formation, suppresses parasitic PC oxidation/reduction, and enables high ionic conductivity with low interfacial resistance for fast Li^+ transport.[36] Molecular dynamics (MD) calculations further highlight the intrinsic differences in solvation structure between the commercial electrolyte (CE, $LiBF_4$ in a PC : DME) and the T-electrolyte. In the CE, the Li^+ solvation sheath is rigid and solvent-dominated in which PC/DME overwhelmingly coordinate Li^+ (PC coordination up to 24.69%) with strong binding energies (6.09–9.23 eV). By contrast, the T-electrolyte exhibits a weakly coordinated, anion-assisted solvation network characterized by a markedly reduced PC coordination (11.76%), additional participation from iBA (5.24%) and FSI^-/$DFOB^-$ anions involvement, enhanced Li–F/Li–O ($DFOB^-$) correlations and lower binding energies (5.41–5.83 eV). Consequently, batteries employing the T-electrolyte retain ~98.4% of their 25°C discharge capacity at −20°C, and sustain stable discharge specific capacities over 500 cycles at 0.2 C and −20°C with a capacity retention of about 90.4%, whereas batteries with the CE exhibit rapid capacity decay and fail after short-term cycling. These results demonstrate that integrating tri-salt chemistry with a weakly solvating ternary solvent system provides an effective design principle for electrolytes that enable wide-temperature operation and long-term cycling stability.

2. Experimental

2.1. Materials

Propylene carbonate (PC, 99.95%, battery grade), 1,2-dimethoxyethane (DME, 99.95%, battery grade), and isobutyl acetate (iBA, 99.9%, anhydrous) were purchased from Dodo Chem Co. Lithium salts, including lithium tetrafluoroborate ($LiBF_4$, 99.9%), lithium bis(fluorosulfonyl)imide (LiFSI, 99.9%), and lithium difluoro(oxalato)borate (LiDFOB, 99.9%) were also obtained from Dodo Chem Co. and used without further purification. The tri-salts electrolyte was prepared by dissolving 0.75 M $LiBF_4$, 0.2 M LiFSI and 0.05 M LiDFOB in a mixed solvent of PC:DME:iBA (v/v/v = 25:65:10). The overall salt concentration and molar ratios were systematically varied to optimize the

composition, designated as the “T-electrolyte”. For comparison, reference electrolyte (CE) composed of 1.0 M $LiBF_4$ in a PC:DME (v/v = 1:1) was employed. $LiCoO_2$ powder (D50 = 6 μm, 99.5%, Ningbo Chuangli New Material Technology Co., Ltd) was utilized without further treatment. Cathode slurry, comprising 70 wt% $LiCoO_2$, 20 wt% poly(vinylidene fluoride) (PVDF, 5130, Solvay), and 10 wt% carbon black (Super C65, Imerys), was cast onto carbon-coated Al foil (18 μm, Showa Denko) using a 150 μm doctor blade. The electrodes were dried under dynamic vacuum at 100°C for 8 h, and punched into 12 mm diameter disks with a geometric area of 1.13 cm2 and mass loading 1.5-2.0 mg cm^{-2}. Lithium foil (200 μm, 99.9%, China Energy Lithium) served as the counter electrode. CR2032-type Li||$LiCoO_2$ coin cellswere assembled in an Ar-filled glove box (H_2O and O_2 < 0.1 ppm) containing 150 μL of electrolyte per cell. After standing at 25°C for 8 h to ensure complete wetting, the batteries were equilibrated in a temperature-programmable chamber (–60 to 120°C, ±0.1°C, model JD-8002-80L, Dongguan Jiedong Test Equipment Co., Ltd.) prior to galvanostatic cycling between 2.8 and 4.2 V using a Neware BTS-4000 battery tester. Electrochemical impedance spectroscopy (EIS, 0.01 Hz to 1 MHz, 5 mV perturbation) and linear-sweep voltammetry (LSV, 0.005 mV s^{-1}) were recorded on a Zahner-class electrochemical workstation (Zhengzhou Shiruisi Instrument Technology Co., Ltd.).

2.2. Characterizations

Raman spectra at –20ºC and ambient temperature (25ºC) were collected using a Thermo Fisher DXR2xi spectrometer equipped with a 785 nm excitation laser. After electrochemical cycling, coin batteries were disassembled in an Ar-filled glove box. $LiCoO_2$ cathodes and Li anodes were gently rinsed with anhydrous DME and subsequently dried under vacuum. After sputter-coating with a ~5 nm-thick Au layer, the pristine and cycled electrodes were examined using a field-emission scanning electron microscope (FE-SEM, Hitachi SU8220) operated at 5 kV and 10 μA. X-ray photoelectron spectroscopy (XPS) was performed on a ULVAC-PHI VersaProbe 4 (Al

Kα, 1486.6 eV) to analyze the surface chemical states. All spectra were calibrated to adventitious C 1s at 284.8 eV and processed using the CasaXPS software package. Phase identification was carried out by X-ray diffraction (XRD, Bruker D8 ADVANCE) employing Cu Kα radiation (40 kV, 40 mA) over a 2θ range of 10-80° with a step size of 0.02°. The viscosities of different electrolyte samples were measured using an Anton Paar MCR102e rheometer over a temperature range from –20°C to 40°C. All viscosity values were directly recorded during a programmed temperature scan. The measurements were performed under a nitrogen atmosphere to minimize moisture and air exposure, and the acquired data were processed using Anton Paar RheoCompass software.

2.3. Theoretical calculations

Density functional theory (DFT) calculations were performed using the DMol^3 module implemented in the Materials Studio package. The B3LYP hybrid functional with Grimme's DFT-D2 dispersion correction and a double numerical plus polarization (DNP 4.4) basis set was employed to describe molecular interactions. All molecular geometries were fully optimized with electrostatic potential (ESP) charge fitting. The *k*-point sampling was restricted to the Gamma (1 × 1 × 1), and the convergence tolerance was set at 1.0×10^{-5} Ha, 2.0×10^{-3} Ha Å^{-1} and 5.0×10^{-3} Å for maximum displacement. The solvation energy (E_{sol}) was calculated using the following expression:

$$\boldsymbol{E_{sol} = E_{total} - E_1 - E_2}$$

where E_{total} denotes the total energy of the solvated system, and E_n represents the energy of individual isolated molecules. Molecular dynamics (MD) simulations were performed using the Forcite module in Materials Studio. The COMPASSIII force field was applied to all simulations with anion charges scaled by 0.7 in accordance with previous studies to account for charge delocalization effects. Two electrolyte models were constructed: (i) a ternary-solvent system (T-box) containing 96 DME, 108 PC, 30 $LiBF_4$, 8 LiFSI, and 2 LiDFOB molecules; (ii) an iBA-containing system comprising

266 DME, 108 PC, 30 $LiBF_4$, 8 LiFSI, and 2 LiDFOB molecules. All systems were equilibrated under the NPT ensemble using the Berendsen barostat (decay constant 0.1 ps) and the Nosé thermostat at 298K for 20 ps. Subsequently, production runs were performed under an NVT ensemble for 200 ps to ensure equilibrium of the electrolyte configurations.

3. Results and discussion

Raman spectroscopy and MD simulations were performed to validate the designed solvation hierarchy of the T-electrolyte and its evolution with temperature. At 25°C, the CE exhibits two dominant Raman bands at ~850 cm^{-1} (νs_{C-O-C} of DME) and ~1780 cm^{-1} ($\nu_{C=O}$ of PC), confirming that Li^+ solvation is mainly governed by DME and PC (**Fig. 1**a). In contrast, the T-electrolyte shows, in addition to the DME band at ~850 cm^{-1}, a distinct $\nu_{C=O}$ band at about 1730 cm^{-1} that persists from 25°C to –20°C (Fig. S1a), which is assigned to iBA and evidences its active participation within solvation shells through weak coordination.[37] In addition, the enlarged Raman spectra in Fig. S1 further experimental support for the regulated local solvation structure of the T-electrolyte. In the 660 to 800 cm^{-1} region, the T electrolyte exhibits a band at around 710 to 715 cm^{-1} that can be assigned to $DFOB^-$ related oxalate and O–B–O vibrations, together with a broadened feature at around 720 to 735 cm^{-1} associated with FSI^- related ionic species. A weak shoulder at ~760–770 cm^{-1} can be attributed to the B–F vibration of BF_4^-. These anion related spectral features are more evident in the T electrolyte than in the CE, supporting the anion-involved solvation structure suggested by the MD analysis. Meanwhile, the PC carbonyl band is markedly attenuated in the T-electrolyte compared with the CE, suggesting that iBA partially replaces PC in the primary solvation sheath and thereby weakens PC-dominated coordination. Especially at lower temperature, the CE consistently displays a stronger PC signal, suggesting that PC-dominated Li^+ solvation becomes more pronounced and thus more susceptible to reductive decomposition, whereas the persistent iBA-associated band in the T-

electrolyte implies that iBA effectively mitigates PC over-coordination and suppresses interfacial side reactions. Furthermore, this sustained ester-involved coordination in the T-electrolyte moderates the overall coordination strength, which is consistent with the absence of solvent-selective crystallization observed experimentally even under subzero conditions (Fig. S2).

Complementary MD simulation snapshots further visualize the distinct liquid structures arising from the different solvation chemistries in the CE and T-electrolyte. As shown in **Fig. 1**b, the CE simulation cell exhibits a liquid environment in which Li^+ is embedded in tightly packed PC/DME coordination spheres with limited configurational flexibility. Conversely, T-electrolyte develops a more heterogeneous spatial distribution, where FSI^- and $DFOB^-$ anions are frequently located in the vicinity of Li^+ and weakly coordinating iBA molecules are interspersed within the primary solvation sheath. This mixed anion/solvent coordination environment is expected to weaken purely solvent-dominated Li^+ solvation, thereby facilitate Li^+ transport by lowering the effective desolvation barrier and providing structural precursors for anion-enriched interphases at electrode surfaces. The radial distribution functions (RDF) offer deeper insights into the spatial organization of solvation structures that correlate with the distinct electrochemical behaviors of two electrolytes. In the CE system, pronounced Li–O (DME) and Li–O (PC) correlations dominate the coordination environments, whereas Li–F (BF_4^-) contacts are comparatively weak (**Fig. 1**c), consistent with a solvent-controlled solvation that tends to restrict ionic mobility, particularly at reduced temperatures where tightly bound solvent networks hinder Li^+ desolvation and promote interfacial instability. As shown in **Fig. 1**d, T-electrolyte exhibits enhanced Li–F (FSI^-) and Li–O ($DFOB^-$) correlations together with a measurable Li–O (iBA) correlations, reflecting an intentionally designed integration of competitive anion coordination and weakly solvating ester molecules that disrupt simple solvent-selective ordering. Such anion-assisted solvation is expected to favor

the formation of inorganic-rich nterphases containing LiF and borate/oxalate-derived species, thereby stabilizing the electrode/electrolyte interface under wide-temperature operation. This structural difference is further quantified by coordination-number analysis (**Fig. 1**e). While solvent-dominated coordination persists (DME: 59.17%, PC: 24.69%) in CE with only a smaller contribution from BF_4^-, T-electrolyte demonstrates a substantial reduction in PC coordination (11.76%) accompanied a non-negligible participation of iBA (5.24%) and anions (BF_4^-/FSI^-/$DFOB^-$ together ~17%). This reconfigured coordination environment provides a structural basis for an inorganic-dominant SEI enriched in fluorinated and oxygen-containing species, which can suppress parasitic reactions and accelerate Li^+ transport kinetics. Representative Li^+ solvation clusters and their corresponding binding energies also reveal the distinct coordination characteristics in the T-electrolyte compared with the CE, and these binding-energy differences more clearly illustrated by the optimized structural models in Fig. S3. For the CE (**Fig. 1**f), representative Li^+-DME/PC clusters exhibit relatively strong binding energies of 6.09–9.23 eV, indicating tightly bound solvation structures that impede Li^+ desolvation and transport, especially under low-temperature conditions

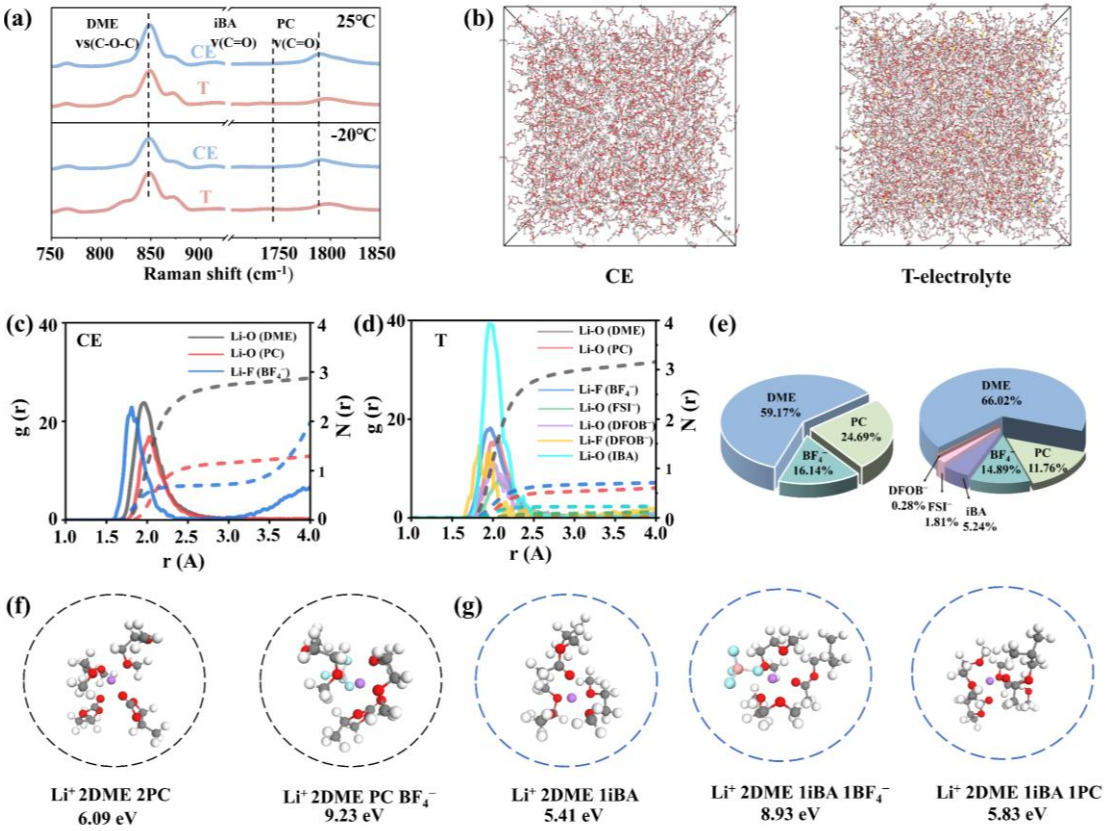

Fig. 1. (a) Raman spectra of CE and T-electrolyte at 25°C and –20°C. (b) MD snapshots of CE and T-electrolyte. RDF of Li^+ with anion/solvent in (c) CE and (d) T-electrolyte. (e) The statistical coordination numbers of Li^+ with anion and solvent. Representative solvation clusters in (f) CE and (g) T-electrolyte and their corresponding binding energies.

where thermal activation is limited. As depicted in **Fig. 1**g, mixed Li^+-anion-solvent clusters characteristic of the T-electrolyte, such as Li^+·2DME·iBA and Li^+·2DME·iBA·PC, display the reduced binding energies of 5.41–5.83 eV, consistent with a more weakly coordinated solvation shell that facilitates Li^+ dissociation. Although certain clusters still possess relatively high binding energy (8.93 eV), the presence and higher population of these lower-energy motifs result in a weaker average solvation strength in the T-electrolyte. Collectively, these spectroscopic and computational results describe the equilibrium ion speciation, revealing that the cryogenic superiority of the T-electrolyte is closely associated with a weakly coordinated and compositionally diversified solvent/anion coordination structure. Specifically, the concurrent incorporation of iBA and multi-anion coordination disrupts

excessive PC participation in the first solvation shell and creates more labile coordination sites along percolated ion transport pathways. Meanwhile, the multidentate $DFOB^-$ anions helps redistribute coordination among multiple oxygen donors and alleviates overcrowding of carbonate molecules around Li^+, whereas the steric bulk of iBA dilutes strong solvent-solvent interactions that would otherwise stabilize tightly bound clusters and elevate the desolvation barrier. Unlike the traditional PC-rich CE, where strongly bound solvation shells become detrimental under thermal and cryogenic extremes, leading to sluggish Li^+ desolvation and unstable interphases, this deliberately heterogeneous coordination enhances interfacial stability and facilitates Li^+ transport, thereby yielding higher ionic conductivity, improved low-temperature kinetics and reduced parasitic reactions.

Therefore, Figure 2a schematically summarizes the contrasting solvation motifs and interphase evolution in the CE and the tri-salt T-electrolyte. In the CE, Li^+ is predominantly coordinated by PC (with DME as a co-solvent), forming a solvent-dominated solvation sheath with a high desolvation penalty that becomes more pronounced at low temperature. This rigid solvation environment promotes continuous solvent decomposition, producing organic-/carbonate-rich interphases, with limited LiF formation and thus elevated interfacial resistance. In contrast, the T-electrolyte reshapes Li^+ solvation through weakly coordinating iBA and competitive coordination from BF_4^- /FSI^-/$DFOB^-$, which partially displaces carbonate solvents in the primary solvation shell and lowers the desolvation barrier. Preferential anion-derived interfacial reactions then are expected to generate compact, inorganic-rich interphases enriched in LiF/$LiSO_xF$/borate-rich containing species, suppressing parasitic solvent reactions and stabilizing electrode interfaces. After establishing the fundamental differences in solvation structures between CE and T-electrolyte, it is essential to clarify how these molecular-level features translate into macroscopic electrochemical kinetics. To this end, temperature-dependent electrochemical impedance spectroscopy (EIS) and ionic

conductivity measurements were performed to quantitatively correlate solvation modulation with ion-transport and charge-transfer behavior. EIS at 25, –20, and 40ºC and fitted using an equivalent circuit model comprising ohmic resistance, interfacial resistance and a Warburg element to describe diffusion processes (Fig. S4).[38] As shown in the Nyquist plots at 25ºC (**Fig. 2**b), batteries employing the T-electrolyte display a much smaller depressed semicircle than those with the CE, and equivalent-circuit fitting yields an interfacial resistance of 68.3 Ω for the T-electrolyte versus 178.2 Ω for the CE, corresponding to a 61.7% reduction, which reflects more facile Li^+ charge transfer at room temperature. This kinetic advantage amplifies under cryogenic condition (**Fig. 2**c), where the T-electrolyte containing $LiBF_4$, LiFSI and LiDFOB with iBA as co-solvent maintains 87.5 Ω interfacial resistance at –20°C compared to CE's 241.3 Ω, representing a 63.7% reduction despite the severe temperature limitation. Even at 40ºC (Fig. S5), the interfacial resistance of cell with the CE rises to 209.2 Ω, indicative of interfacial degradation, while that of the T-electrolyte decreases to 57.6 Ω, corresponding to a remarkable 72.5% reduction, further confirming its ability to maintain low-resistance interfaces at elevated temperature. The consistently smaller high-frequency intercepts and reduced semicircle diameters for the T-electrolyte confirm that the tri-salts formulation affords both lower bulk resistance and faster interfacial charge-transfer kinetics,[39] in good agreement with its higher ionic conductivity measured independently. The ionic conductivities of both electrolytes were further evaluated over a broad temperature range (**Fig. 2**d). While CE follows typical Arrhenius-type trend, with conductivity declining from 5.0 mS cm^{-1} at 40ºC to 3.4 mS cm^{-1} at –20ºC, the T-electrolyte demonstrates exceptional conductivity resilience, maintaining 4.73 mS cm^{-1} at –20ºC. This represents 91.0% retention of its room-temperature conductivity (5.2 mS cm^{-1} at 25ºC), whereas the CE retains only 73.5% of its 25ºC conductivity over the same temperature interval. Notably, the T-electrolyte achieves higher conductivity than CE throughout the operational range,

most critically delivering a substantial enhancement at the challenging –20°C benchmark and still outperforming the CE at 40°C (7.0 *vs.* 5.0 mS cm^{-1}). The enhanced ionic conductivity of the T-electrolyte can be attributed to the combined effect of reduced viscosity and regulated solvation structure regulation. On the one hand, the PC/DME/iBA solvent matrix helps maintain liquid phase ion mobility by alleviating viscosity related transport limitations, which become more pronounced at low temperature. On the other hand, conductivity is not governed by viscosity alone, but also depends on salt dissociation, the fraction of effectively mobile Li^+ species and the strength of Li^+ coordination. The incorporation of iBA, together with the participation of multiple anions, weakens the PC dominated Li^+ solvation sheath and reduces excessive solvent binding around Li^+, while maintaining sufficient anion involvement for interphase forming chemistry. As a result, the T-electrolyte maintains both favorable ion mobility and a more labile Li^+ coordination environment, leading to higher low-temperature conductivity and faster interfacial charge transfer. Such dual-temperature superiority in both cryogenic and elevated-temperature regimes is consistent with the solvation and interphase chemistry discussed above that LiDFOB-derived borate and oxalate species together with LiFSI-derived fluorinated components promote the formation of mechanically robust, LiF-rich interphases, while the weakened, anion-participating solvation structure lowers the Li^+ desolvation barrier and maintains high bulk ion availability, collectively enabling rapid Li^+ transport and stable charge transfer under wide-temperature operation.

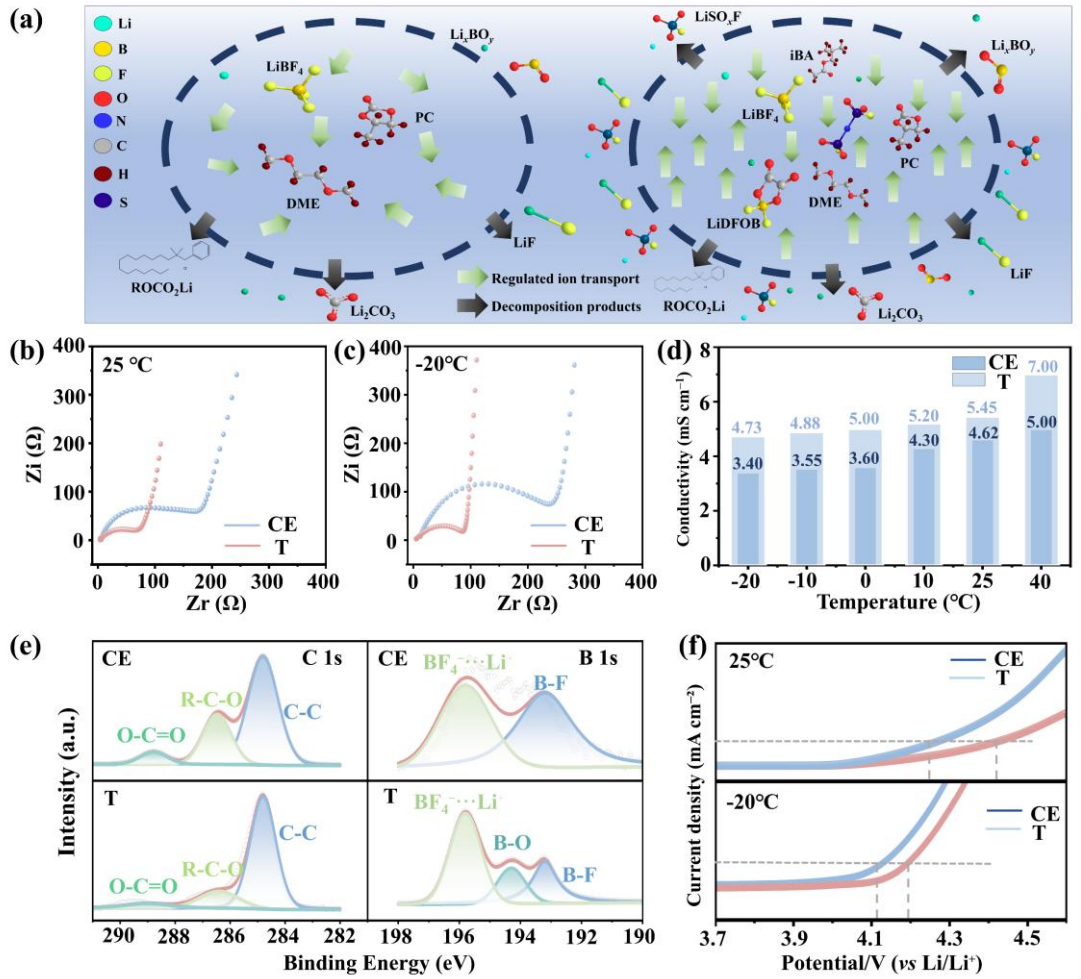

Fig. 2. (a) Schematic comparison of solvation structures and interphase evolution in the CE and the T-electrolyte. EIS spectra for CE and T-electrolyte at (b) 25°C and (c) –20°C. (d) Conductivity as a function of temperature for CE and T-electrolyte. (e) XPS spectra of C 1s and B 1s for CE and T-electrolyte. (f) LSV curves at 25°C and –20°C for CE and T-electrolyte.

X-ray photoelectron spectroscopy (XPS) was used for compositional analysis (Fig. S6) both the CE and T-electrolyte. In the C 1s spectra (**Fig. 2**e, left), both electrolytes display characteristic components at approximately 284.8 eV (C–C), 286.4 eV (R–C–O) and 289.0 eV (O–C=O), arising from the organic carbonate and ether solvents.[28] In the CE system, the O–C=O and R–C–O peaks are relatively intense, indicating a large fraction of PC-derived carbonate environments in which carbonyl oxygen atoms strongly interact with Li^+, consistent with a PC-rich, strongly coordinating solvation shell. In contrast, the T-electrolyte shows a weaker O–C=O contribution and a broader R–C–O peak, suggesting reduced PC involvement and an increased contribution from

DME/iBA-derived environments, in line with the DME/iBA-dominated and anion-participating solvation structure revealed by Raman and MD analyse. This shift from a strongly PC-coordinated solvation environment to a more weakly coordinated mixed-solvent environment is expected to render the local liquid structure more flexible, thereby facilitating Li^+ mobility and suppressing PC over-reduction at low temperature. The B 1s spectra (**Fig. 2**e, right) further highlight the differences in anion chemistry between the two electrolytes. For the CE, B 1s can be deconvoluted into two main components at 193.2 eV (B–F) and 195.8 eV ($BF_4^-\cdots Li^+$ contact ion pairs), which are typical features of a single-salt $LiBF_4$ electrolyte and indicate that B–F bonding environments dominate.[40] By contrast, the T-electrolyte shows a more complex B 1s spectrum with three components located at 193.2 eV (B–F), 194.3 eV (B–O species originating from $DFOB^-$) and 195.8 eV ($BF_4^-\cdots Li^+$), confirming the coexistence of B–F and B–O environments in a multi-anion coordination framework. The appearance of B–O species, together with the synergistic participation of FSI^- and $DFOB^-$ evidenced by F 1s spectra (Fig. S7), increases both the diversity and stability of the Li^+-anion coordination motifs and supports the formation of an anion-rich, weakly coordinated solvation structure. Such a controlled solvation environment in the T-electrolyte is fully consistent with its reduced desolvation barrier and LiF/borate-forming interphase chemistry discussed above, thereby providing a molecular-level rationale for the enhanced interfacial kinetics and superior low-temperature conductivity retention observed in the EIS and conductivity measurements. Furthermore, linear sweep voltammetry (LSV) was employed to evaluate the stability of the two electrolytes. At ambient temperature of 25°C, the oxidation onset potential of the T-electrolyte, defined at a current density of 20 mA cm^{-2}, is shifted positively by +0.19 V decomposition onset potential shift relative to that of the CE (**Fig. 2**f), indicating a wider oxidative stability window at room temperature. Under the more demanding low-temperature condition of –20°C, the T-electrolyte still exhibits a higher oxidation onset, with an additional

~0.1 V positive shift compared with the conventional electrolyte. These results demonstrate that the T-electrolyte maintains superior anodic stability over a wide temperature range, which is favorable for sustaining high-voltage operation without triggering premature electrolyte oxidation.

To determine whether the molecular-level advantages of the T-electrolyte translate into practical cell-level benefits, the two electrolytes were further evaluated in Li||$LiCoO_2$ batteries with a focus on cycling stability, rate capability and low-temperature performance. A series of tri-salts electrolytes featuring distinct ratios of $LiBF_4$, LiFSI and LiDFOB were carefully formulated and tested under both ambient (25°C) and low-temperature (−20°C) conditions. As shown in **Fig. 3**a, the T-electrolyte containing 0.75 M $LiBF_4$, 0.2 M LiFSI and 0.05 M LiDFOB in a PC : DME : iBA (25 : 65 : 10 by volume, Fig. S8) solvent mixture delivers outstanding room-temperature cycling stability, retaining approximately 138.6 mAh g^{-1} after 200 cycles at 0.2 C with Coulombic efficiency consistently exceeding 99.5%. In contrast, alternative tri-salt formulations exhibit faster capacity fading and lower Coulombic efficiencies, underscoring the importance of carefully balancing the three salt components. Under the more demanding low-temperature condition of −20℃ (**Fig. 3**b), the same 0.75 M $LiBF_4$ + 0.2 M LiFSI + 0.05 M LiDFOB formulation maintains a high discharge capacity of 133.2 mAh g^{-1} at 0.2 C, whereas batteries using other compositions suffer pronounced capacity decay. The superior cryogenic performance of this optimized T-electrolyte can be primarily attributed to its well-balanced solvation structure and synergistic multi-anion coordination that LiFSI and LiDFOB anions effectively compete with PC for Li^+ coordination sites, partially displacing PC from the primary solvation shell, suppressing solvent decomposition, and facilitating Li^+ transport. By contrast, an excessively high LiDFOB content (e.g., 0.7 M $LiBF_4$ + 0.2 M LiFSI + 0.1 M LiDFOB) electrolyte may strengthen Li^+ anion association and increases the electrolyte viscosity, thereby lowering the fraction of effectively mobile Li^+ species and

slowing ion transport at low temperature (Fig. S9). Therefore, a moderate LiDFOB level combined with an optimized $LiBF_4$/LiFSI ratio is essential for achieving a favorable balance between ion transport and stable electrode/electrolyte interfaces at low temperature. These synergistic effects weaken Li^+ desolvation barriers, optimize ion-transport pathways and stabilize electrode interfaces under cryogenic conditions, as will be further corroborated in the following sections. The voltage-capacity profiles provide direct evidence linking electrolyte formulation to electrode reaction kinetics. For the reference electrolyte (CE, 1.0 M $LiBF_4$ in PC : DME = 1:1 v/v), severe voltage polarization is observed at both 25℃ (**Fig. 3**c) and −20℃ (**Fig. 3**d), as reflected by the large charge/discharge hysteresis and the progressive sloping of the plateaus with cycling, indicative of increasing kinetic limitations and growing interfacial resistance. Conversely, Li||$LiCoO_2$ batteries employing the optimized T-electrolyte displayed well-defined and tightly overlapping charge/discharge plateaus both temperatures (**Fig 3**e and **3**f), with a smaller voltage gap and more stable mid-plateau potentials, suggesting markedly alleviated polarization, more facile Li^+ diffusion, and sustained charge-transfer kinetics even under cryogenic conditions. Rate capability testing further accentuate the differences in charge-transport behavior between the two electrolytes. At 25℃ (**Fig. 3**g), the CE formulation exhibited specific capacities of 117.5, 105.6, 84.8, 58.3, 44.0, 30.1 and 18.7 mAh g^{-1} at 0.1, 0.2, 0.5, 1, 2, 5 and 10 C, respectively, and recovered to 114.6 mAh g^{-1} when the rate is returned to 0.1 C. The T-electrolyte formulation (**Fig. 3**h) provides a much higher baseline capacity of 133.5 mAh g^{-1} at 0.1 C. Moreover, after being cycled up to 10 C and subsequently returned to 0.1 C, the cell with the T-electrolyte almost completely recovers its initial capacity, with ~100% retention of the original 0.1 C value, demonstrating excellent rate reversibility. This kinetic advantage is preserved at −20℃ (**Fig. 3**i and **3**j), where T-electrolyte still delivers 132.6 mAh g^{-1} at 0.1 C, and preserves a substantial discharge capacity at the demanding 0.4 C rate at which the CE cell nearly loses its capacity output. Furthermore,

upon returning from high-rate cycling at subzero temperatures to 0.1 C, the T-electrolyte exhibits excellent reversibility, recovering a capacity of 112.9 mAh g^{-1}. Even at elevated temperature (40°C), additional electrochemical evaluation (Fig. S10) shows that the T-electrolyte maintains a reversible capacity of 109.8 mAh g^{-1} at 0.2 C after 200 cycles with Coulombic efficiency consistently above 99.7%. In contrast, the CE exhibits the irregular capacity fluctuations after 80 cycles followed by rapid failure, indicating an unstable electrode/electrolyte interface. The corresponding rate performance at 40°C (Fig. S11) also confirms that the T-electrolyte sustains high reversible capacities even under 5-10 C operation, whereas the CE system suffers from severe polarization and poor rate adaptability. Even under higher current density of 5.0 C, the cycling stability of the T-electrolyte remains markedly superior to that of the CE (Fig. S12). The higher current density long-term cycling tests at different temperatures further represent fast charge/discharge scenarios and directly evaluate the high-rate tolerance of the electrolyte. Li||Li symmetric cells further employed to evaluate the compatibility of the T-electrolyte. At both 25°C and −20°C, the T-electrolyte shows lower voltage hysteresis and more stable Li plating/stripping behavior than the CE (Fig. S13). Such rate resilience stems directly from the tri-functional interfacial architecture engineered in our T-electrolyte formulation. LiDFOB decomposition yields boron-oxygen networks that form uniform, mechanically robust, fluorine- and borate-rich SEI/CEI layers capable of accommodating rapid lithiation/delithiation without loss of interfacial integrity. Simultaneously, LiFSI generates fluoride-rich interphases that reduce interfacial resistance and suppress localized interfacial reactions. Together with the stabilizing contribution of $LiBF_4$ at high voltage, these interfacial chemistries collectively support fast Li^+ transport and highly reversible charge storage over a wide range of current densities and temperatures. Long-term cycling further highlights the robustness of the tri-salt formulation at both ambient and subzero temperature. **Fig. 3**k

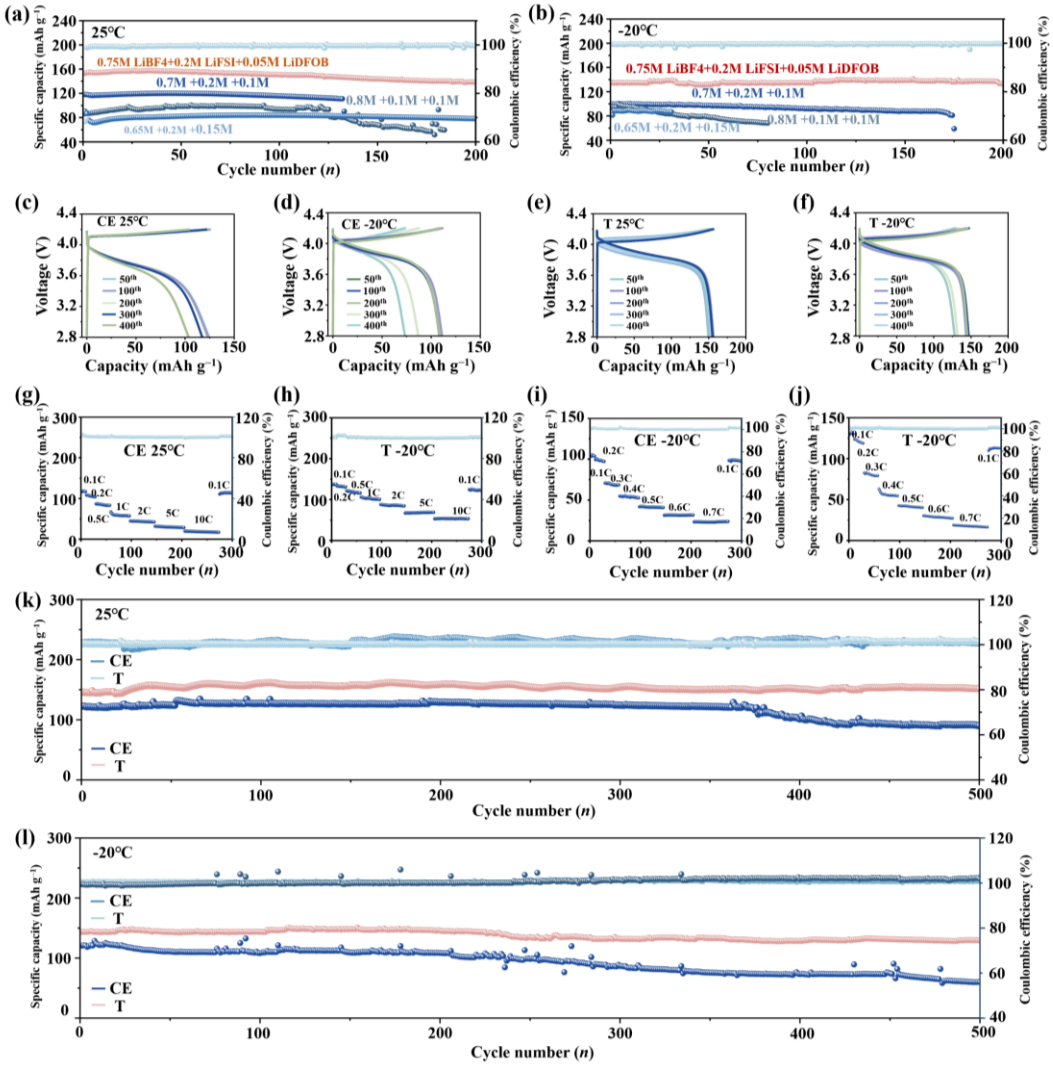

Fig. 3. Specific capacity and coulombic efficiency at (a) 25°C and (b) −20°C over 200 cycles for different electrolyte compositions. Galvanostatic charge/discharge curves of Li||$LiCoO_2$ batteries at (c and e) 25°C and (d and f) −20°C for the different cycles. Rate performance of (g) CE and (h) T-electrolyte at 25°C. Rate performance of (i) CE and (j) T-electrolyte at −20°C. Long-term cycling performance at (k) 25°C and (l) −20°C for both electrolytes.

shows that at 25°C, Li||$LiCoO_2$ batteries with the the CE show gradual capacity fading from an initial discharge capacity of 122.5 mAh g^{-1} to at 90.5 mAh g^{-1} after 500th cycles, while the T-electrolyte sustain 151.7 mAh g^{-1} over the same period, slightly exceeding its initial capacity and corresponding to ~100% capacity retention due to mild activation. At −20°C (**Fig. 3**l), the advantage of the T-electrolyte becomes even more pronounced. Its initial discharge capacity reaches 143.5 mAh g^{-1}, corresponding to ~98.4% retention relative to its room-temperature value, while after 500 cycles it still preserves 129.7

mAh g^{-1}, ~85.5% of its room-temperature capacity. However, CE suffers catastrophic degradation to 47.2 mAh g^{-1} after 500 cycles at −20°C. A comparison of specific capacity and Coulombic efficiency at 25 and −20°C thus shows that the T-electrolyte consistently outperforms the CE, with particularly striking gains in capacity retention and efficiency under cryogenic conditions. For further comparison, a commonly used carbonate electrolyte, 1 M $LiPF_6$ in EC/DEC, was also evaluated in Li||$LiCoO_2$ battery (Fig. S14). At −20°C and 0.2 C, the discharge capacity decreases from 71.4 to 55.2 mAh g^{-1} after 100 cycles, demonstrating that the T-electrolyte provides a clear advantage over the conventional carbonate based $LiPF_6$ electrolyte under subzero condition. Such exceptional low-temperature endurance arises from the synergistic interplay of the three distinct lithium salts in the T-electrolyte, each contributing complementary functionality. Meanwhile, the precisely balanced PC : DME : iBA (25 : 65 : 10 by volume) solvent system optimizes the Li^+ solvation shell by combining strong dielectric screening with weakened, anion-participating coordination, thereby lowering desolvation barriers, facilitating fast ion transport, and reducing internal resistance at subzero temperatures.

Although the electrochemical measurements highlight substantial performance differences between the two electrolytes, their origins must be clarified from the perspective of interfacial chemistry. Therefore, high-resolution XPS analyses of cycled Li anodes were conducted to resolve the SEI compositions formed under both ambient and cryogenic conditions (**Fig. 4**). The C 1s spectra can be deconvoluted into typical SEI-related components at 284.8 eV (C–C), 286.8 eV (R–C–O), 289.0 eV (O–C=O) and 289.8 eV (CO_3^{2-} in inorganic/organic carbonates).[41] For cells using the CE at 25ºC (**Fig. 4**a, top), the O–C=O and CO_3^{2-} peaks are highly intense, indicating extensive formation of organic carbonate species and solvent-decomposition fragments that give rise to an organics-rich SEI on Li. When the same electrolyte is cycled at –20ºC (**Fig. 4**b, top), these carbonate-associated signals remain strong or even increase,

evidencing persistent low-temperature solvent reduction and the growth of a thicker, more heterogeneous organics-dominated SEI that is prone to continuous electrolyte consumption. In contrast, Li anodes cycled in the T-electrolyte (**Fig. 4**a and b, bottom) exhibit markedly attenuated O–C=O and CO_3^{2-} components together with a relatively greater contribution from the C–C/R–C–O region, implying suppressed carbonate-forming decomposition and a more compact SEI. Semi-quantitative peak-area analysis (Table S2) shows that at –20ºC the O–C=O and CO_3^{2-} contributions are reduced by approximately 6.48% and 2.27%, respectively, compared with the CE, indicating a modest but systematic suppression of carbonate-forming side reactions. This chemoselective stabilization is consistent with the weakly coordinating iBA and the anion-participating solvation/interphase chemistry of the T-electrolyte, in which reduced PC participation and LiFSI/LiDFOB-derived interphases mitigate uncontrolled solvent reduction under cryogenic conditions.

In the Li 1s region (**Fig. 4**c and **4**d), the anode cycled in CE at 25°C can be deconvoluted into components assigned to 52.6 eV (Li), 55.4 eV (Li_2CO_3), 56.1 eV (LiF) and 56.8 eV (Li*x*BO*y*), indicating the presence of $LiBF_4$ decomposition products and limited inorganic fluoride formation.[42] The relatively weak LiF contribution compared with Li_2CO_3 suggests that only a limited fraction of the SEI is converted into an inorganic fluoride-rich phase. When cycled at –20°C, the Li_2CO_3 and Li*x*BO*y* features remain dominant and the LiF component does not increase appreciably, suggesting that dense, LiF-rich passivation is difficult to establish under cryogenic conditions and that the Li surface remains largely covered by carbonate-rich products. In contrast, Li anodes cycled in the T-electrolyte exhibit a substantially enhanced LiF component at both 25°C and –20°C, accompanied by reduced Li_2CO_3 intensity and additional high-binding-energy contributions that can be ascribed to LiSO*x*F species (from FSI^-) and Li*x*BO*y* borates (from $DFOB^-$/BF_4^-). Semi-quantitative analysis (Table S3) shows that the LiF fraction in the T-electrolyte is significantly higher than in the

CE, especially at –20°C, supporting the formation of a LiF-enriched inorganic SEI. Such a LiF-rich interphase, reinforced by borate-related species, is expected to provide a mechanically robust and ionically conductive passivation layer that lowers interfacial resistance, mitigates dendritic Li growth (Fig. S15), and thereby enhances low-temperature Li^+ transport, consistent with the EIS and cycling results discussed above.

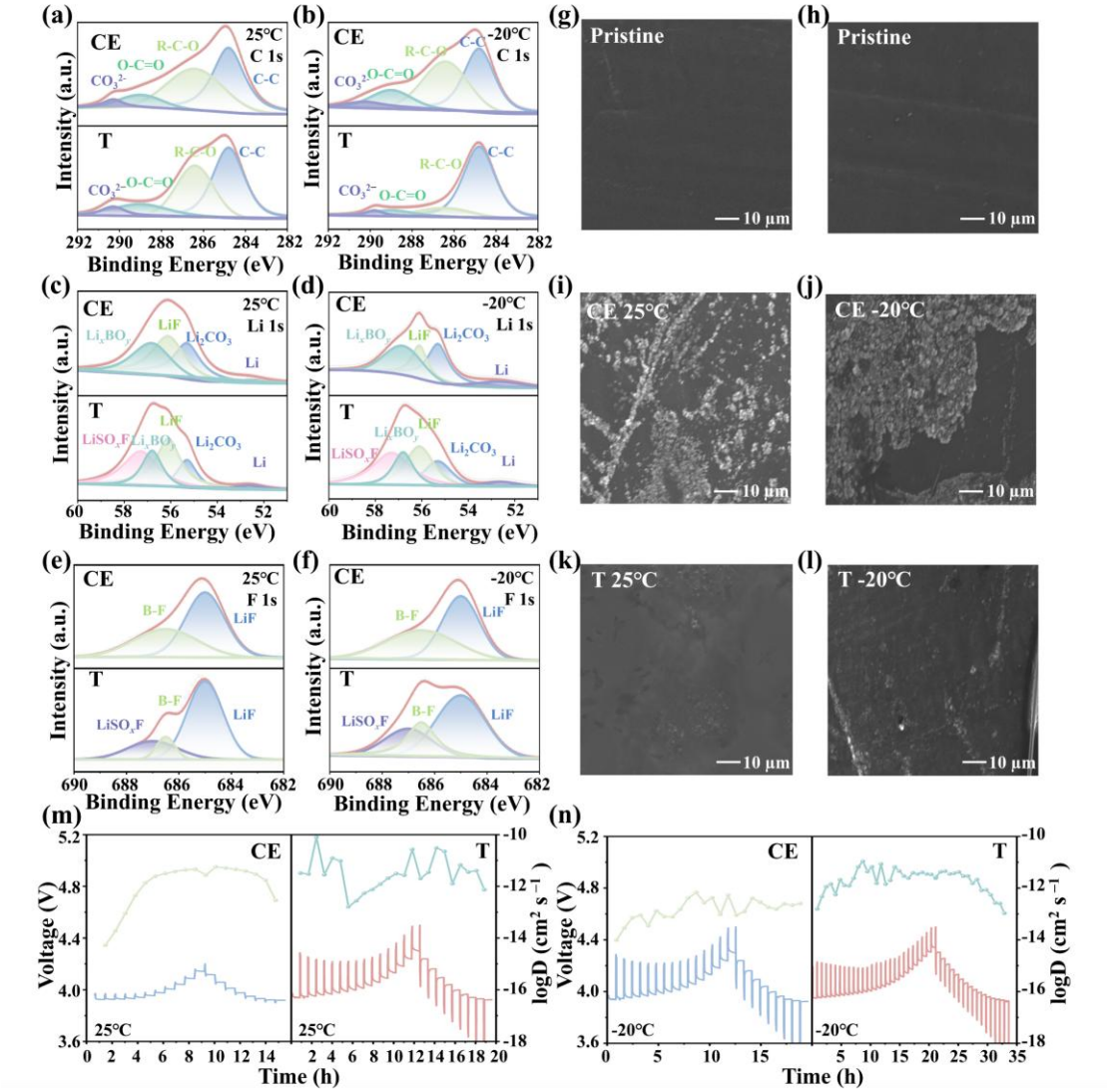

Fig. 4. High-resolution XPS spectra of Li anodes after cycled in CE and T-electrolyte. C 1s spectra at (a) 25°C and (b) –20°C. Li 1s spectra at (c) 25°C and (d) –20°C. F 1s spectra at (e) 25°C and (f) –20°C. SEM images of pristine Li anode at (g) 25°C and (h) –20°C. SEM image of Li anodes cycled in CE at (i) 25°C and (j) –20°C. SEM image of Li anodes cycled in T-electrolyte at (k) 25°C and (l) –20°C. Galvanostatic intermittent titration technique (GITT) profiles of Li‖$LiCoO_2$ batteries employing CE and T-electrolyte at (m) 25°C and (n) –20°C.

The F 1s spectra further supports the compositional advantages of the T-electrolyte under cryogenic operating conditions. As depicted in **Fig. 4**e and **4**f, the F 1s spectra from batteries with the CE at both 25℃ and –20°C are dominated by a B–F component at 686.2 eV arising from BF_4^--derived species, whereas the LiF peak at 685.0 eV is comparatively weak, indicating that only a limited fraction of fluorine is converted into inorganic LiF.[26] In contrast, Li anodes cycled in the T-electrolyte show a strongly suppressed B–F species while establishing an overwhelmingly dominant LiF phase that constitutes 67.70% and 65.02% of F-containing species at 25℃ and –20°C(Table S4). Moreover, an additional higher-binding-energy feature near 687.1 eV can be assigned to $LiSO_xF$ species generated from FSI^--derived interphase products. This evolution becomes even more pronounced upon low-temperature cycling, where the LiF and $LiSO_xF$ signatures in the T-electrolyte become more pronounced, consistent with an increasingly inorganic-rich SEI on the Li surface. Such an LiF-rich interphase, reinforced by sulfate/borate-related species, is expected to form a compact and chemically robust passivation layer that suppresses further solvent reduction and electron leakage, provides more stable interfacial Li^+ transport pathways, lowers interfacial resistance and promotes stable Li deposition, thereby protecting the Li anode against low-temperature degradation in good agreement with the electrochemical results. To further probe the origin of the improved cycling stability at 40°C, XPS spectra were collected from the Li anodes after cycling, as shown in Fig. S16. For the CE, the C 1s spectrum (Fig. S16a) shows pronounced organic oxygen containing components and carbonate species, suggesting persistent solvent decomposition and accumulation of organic and carbonate-derived species at elevated temperature. The corresponding Li 1s (Fig. S16b) and F 1s (Fig. S16c) spectra reveal the coexistence of LiF, Li_2CO_3, Li_xBO_y and B–F-related species, indicating that the SEI formed in CE contains appreciable carbonate and organic decomposition products together with inorganic salt decomposition species. In contrast, the T-electrolyte exhibits

comparatively weaker carbonate-related components in C 1s spectra, while the Li 1s and F 1s spectra exhibit stronger LiF signals together with discernible $LiSO_xF$ and borate-related species. These results indicate that the T-electrolyte still maintains a more inorganic-rich and chemically robust SEI at 40ºC.

To correlate interfacial chemistry with the morphological stability of Li deposition, SEM was performed on Li metal anodes after cycling. The pristine Li surface shows a relatively smooth and featureless morphology at both 25°C and –20°C (**Fig. 4**g and **Fig. 4**h), serving as the baseline state prior to electrochemical cycling. After cycling in the CE, the Li surface becomes severely roughened at 25°C and is covered with non-uniform, porous/mossy deposits with abundant protrusions (**Fig. 4**i). This morphological heterogeneity is further exacerbated at –20°C (**Fig. 4**j), where larger agglomerated deposits and more severe topographical inhomogeneity are observed, indicative of uneven Li nucleation and growth under cryogenic conditions. These features are consistent with the XPS results, which show a carbonate-rich and mechanically less robust SEI in the CE that is less effective in maintaining stable interfacial Li^+ transport. In contrast, Li anodes cycled in the T-electrolyte display substantially improved surface integrity (**Fig. 4**k and **Fig. 4**l). At 25°C, the deposited Li appears comparatively more compact and continuous with suppressed porous/mossy features. Importantly, even at –20°C the Li surface remains denser and more uniform, with significantly fewer large protrusions than that in the CE counterpart. Collectively, these observations support that the LiF-rich, inorganic-dominated SEI formed in the T-electrolyte enables more stable interfacial Li^+ transport and suppresses localized interfacial reactions, thereby suppressing dendrite-like growth and corroborating the superior low-temperature cycling stability of the T-electrolyte.

Based on the galvanostatic intermittent titration technique (GITT) measurements, the Li^+ diffusion kinetics of batteries employing CE and T-electrolytes was compared at both 25°C and –20°C. At 25°C (**Fig. 4**m), both electrolytes exhibit relatively high

lithium-ion diffusion coefficients with D_{Li^+} on the order of 10^{-11} cm^2 s^{-1}, yet the CE exhibits a markedly broader spread and stronger time and state dependence than the T-electrolyte over the full charge and discharge trajectory, implying more heterogeneous transport kinetics and stronger sensitivity to the evolving interphase during cycling even at 25ºC. Upon cooling to –20ºC (Fig. 4n), the apparent D_{Li^+} values of both systems decrease substantially, with the CE spanning roughly the 10^{-12} to 10^{-15} cm^2 s^{-1} regime and showing pronounced downward excursions, whereas the T-electrolyte remains mainly in the 10^{-12} to 10^{-13} cm^2 s^{-1} regime with a narrower dispersion, making the contrast between the two electrolytes more evident. Compared with the CE, the T-electrolyte sustains systematically higher D_{Li^+} across the measured potential window with weaker SOC-dependent fluctuation, while the CE exhibits more pronounced D_{Li^+} deterioration near the high-voltage region and toward deep discharge, consistent with stronger state-dependent transport bottlenecks under subzero operation. Collectively, the broader D_{Li^+} span and stronger fluctuations observed for the CE, together with the higher and more stable D_{Li^+} profiles maintained by the T-electrolyte, support that anion-participating solvation and a more regulated interphase reduce transport intermittency and alleviate low-temperature kinetic penalties, thereby favoring Li^+ transport under both ambient and subzero conditions.

Because the CEI is also critical for wide-temperature operation, high-resolution XPS was performed on $LiCoO_2$ cathodes after cycling in the CE and T-electrolyte at both 25 and –20ºC (**Fig. 5**). The C 1s spectra reveal pronounced differences in CEI composition between the two electrolytes. The deconvoluted C 1s spectra can be mainly described by four contributions. The peak at 284.8 eV is assigned to C–C, which reflects carbonaceous backbones and residual organic species. The component centered at 286.4 eV corresponds to R–O–C, typically arising from ether-/ester-type fragments generated upon solvent decomposition. The O–C=O/$ROCO_2Li$ signals at 288.8 eV and 290.8 eV are attributable to carbonate/semicarbonate species, which represent key constituents of the CEI. Importantly, $ROCO_2Li$-type semicarbonates are not merely parasitic by-products on the cathode. When formed in a controlled manner, $ROCO_2Li$ can act as a

compliant organic scaffold that improves film conformality and mechanical tolerance, alleviates interfacial cracking upon cycling, and provides polar carbonate motifs that facilitate Li^+ transport while blocking direct contact between the electrolyte and the highly oxidative cathode surface.[43] At 25ºC (**Fig. 5**a, top), the CE exhibits pronounced R–O–C and O–C=O signals, indicating substantial accumulation of solvent-derived organic by-products accompanied by the formation of carbonate species at the cathode surface. In contrast, the cathode cycled in the T-electrolyte at 25ºC (bottom panel) shows markedly attenuated intensity R–O–C together with suppressed O–C=O contributions, yet a relatively strengthened $ROCO_2Li$ component is evident, suggesting that the T-electrolyte redirects interfacial reactions toward more selective semicarbonate formation rather than uncontrolled oligomeric/ether-rich decomposition. Such a $ROCO_2Li$-enriched but less R–O–C-dominated CEI is expected to be more conformal and mechanically resilient, thereby stabilizing the cathode surface while limiting continuous electrolyte consumption[44]. Upon cooling to –20ºC (**Fig. 5**b, top), the CE displays a further increase in the R–O–C component (31.64% of the total C elements, Table S5), suggesting aggravated interfacial side reactions under cryogenic conditions and the buildup of an organic-/carbonate-enriched CEI. By contrast, the T-electrolyte (**Fig. 5**b, bottom) maintains substantially weaker O–C=O and R–O–C signals, while the C–C component becomes comparatively more prominent. Meanwhile, the $ROCO_2Li$ contribution remains appreciable and is higher than that in CE, supporting that the tri-salt/ternary-solvent chemistry enables a self-limited CEI where $ROCO_2Li$ semicarbonates provide the organic scaffold and other unstable organics are suppressed. In the Li 1s region (**Fig. 5**c and **5**d), $LiCoO_2$ cathodes cycled within the CE show a dominant Li_2CO_3 contribution (55.4 eV) accompanied by a weaker LiF (56.1 eV) component, indicating a carbonate-rich CEI with only modest inorganic fluoride content. At –20°C, semi-quantitative fitting yields a LiF fraction of ~29.09% of the total Li signal (Table S6), suggesting that conversion of Li-containing interphase species into LiF remains limited under low-temperature. By contrast, the T-electrolyte markedly reshapes the CEI chemistry at 25°C, generating a LiF matrix constituting 42.37% of Li species, accompanied by reduced Li_2CO_3 intensity and an additional higher-binding-energy contribution which is attributed to Li_xBO_y borates

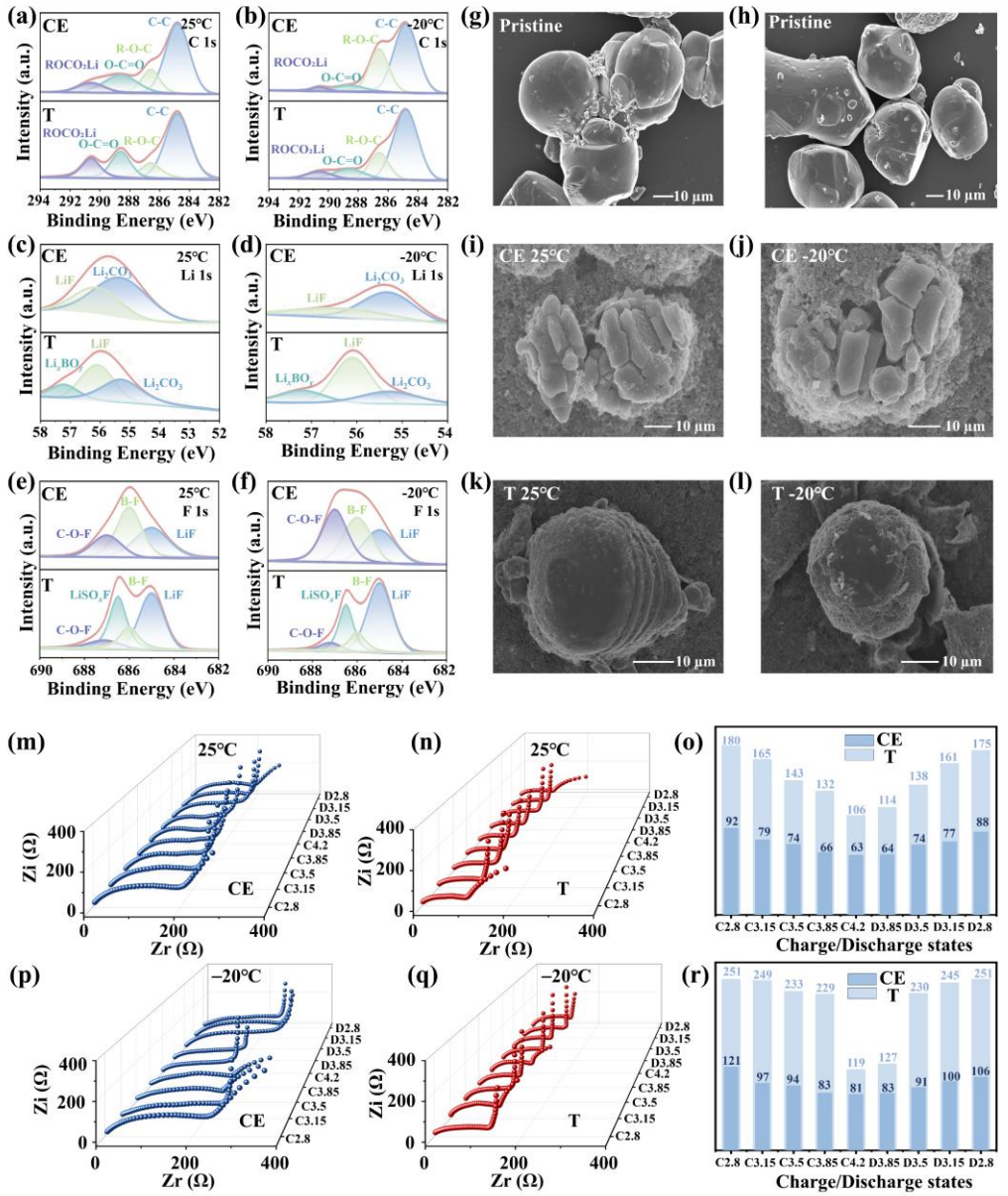

Fig. 5. High-resolution XPS spectra of $LiCoO_2$ cathodes after cycled in CE and T-electrolyte. C 1s spectra at (a) 25°C and (b) –20°C. Li 1s spectra at (c) 25°C and (d) –20°C. F 1s spectra at (e) 25°C and (f) –20°C. SEM images of pristine $LiCoO_2$ at (g) 25°C and (h) –20°C. SEM images of $LiCoO_2$ cathodes cycled in CE at (i) 25°C and (j) –20°C. SEM images of $LiCoO_2$ cathodes cycled in T-electrolyte at (k) 25°C and (l) –20°C. *Ex situ* EIS Nyquist plots of batteries with CE at (m) 25°C and (p) –20°C. *Ex situ* EIS Nyquist plots of batteries with T-electrolyte at (n) 25°C and (q) –20°C. Corresponding interfacial resistance evolution at different charge/discharge states at (o) 25°C and (r) –20°C.

near 57.2 eV originating from boron-containing anions[45]. Importantly, at –20°C the LiF fraction in the T-electrolyte further increases to 53.75% of the Li 1s spectral weight, supporting that the tri-salt formulation promotes LiF formation and sustains a more

inorganic, LiF-enriched passivation layer on $LiCoO_2$ even under harsh low-temperature conditions. As for the F 1s spectra, for batteries cycled with CE, three components can be resolved at both 25ºC and –20ºC (**Fig. 5**e and **Fig. 5**f) that the LiF at 685.0 eV, B–F component at 686.2 eV, and C–O–F-type oxyfluoride contribution at 687.1 eV. At 25ºC (**Fig. 5**e, top), the spectrum is dominated by B–F, while LiF is relatively weak and C–O–F is detectable, indicating that a substantial fraction of fluorine remains in BF_4^--related environments and that fluorinated oxyfluoride/fluorinated organic products are already present in the CEI.[46] Upon cooling to –20ºC, the LiF and C–O–F contributions become more pronounced whereas the relative B-F intensity decreases, consistent with aggravated parasitic interfacial reactions and the accumulation of less stable fluorinated species in the CEI. In contrast, $LiCoO_2$ cathodes cycled in the T-electrolyte exhibit an F 1s profile dominated by LiF, together with a moderate $LiSO_xF$ component near 687.0 eV arising from FSI^--derived interphase products, while B–F and C–O–F signals are strongly suppressed at both temperatures (**Fig. 5**e and **5**f, bottom). Peak-area analysis (Table S7) confirms that LiF constitutes the majority of F-containing species in the T-electrolyte at both 25 and –20ºC, evidencing the formation of a LiF-rich, $LiSO_xF$-reinforced inorganic CEI. Such an F-rich interphase is expected to suppress further electrolyte oxidation and fluorinated organic by-product formation, maintain interfacial integrity, and provide more homogeneous Li^+ transport pathways, thereby lowering interfacial resistance and mitigating low-temperature charge-transfer limitations, consistent with the improved cycling stability of the T-electrolyte. In this tri-salt design, variations in the $LiBF_4$/LiFSI ratio further influence this balance by changing the relative contributions of BF_4^- and FSI^- to ion transport and interphase formation. LiFSI contributes to salt dissociation, ionic conductivity and LiF/$LiSO_xF$-rich interphase formation; therefore, insufficient LiFSI weakens both ion transport and FSI^--derived interfacial stabilization. Meanwhile, $LiBF_4$ serves as the dominant salt component and contributes BF_4^- derived boron and fluorine interfacial species, whereas an inappropriate $LiBF_4$/LiFSI ratio can disturb the balance among effective Li^+ availability, salt dissociation and interphase chemistry. Therefore, the optimized 0.75 M $LiBF_4$ + 0.2 M LiFSI + 0.05 M LiDFOB composition provides the most favorable compromise among ion transport, viscosity control, anion derived interphase chemistry

and stable interface formation. These XPS results also explain why the $LiBF_4$/LiFSI ratio is critical in the tri-salt formulation. Changing this ratio would alter the relative contribution of BF_4^--derived boron/fluorine species and FSI^--derived LiF/$LiSO_xF$ components, thereby affecting the balance between inorganic interphase formation, interfacial resistance and long-term cycling stability.

Beyond the chemical signatures resolved by XPS, morphological evidence from SEM further corroborates the distinct CEI formation behaviors induced by the two electrolyte. Pristine $LiCoO_2$ electrodes show well-defined densely packed secondary particles with relatively smooth surfaces at both 25 and –20°C (**Fig. 5**g and **Fig. 5**h). After cycling in the CE (**Fig. 5**i and **Fig. 5**j), pronounced surface deterioration is observed. At 25°C, the secondary particles become visibly roughened and are partially covered by irregular deposits, suggesting continuous accumulation of electrolyte-derived decomposition products. At –20°C, the degradation is exacerbated, with increasingly blurred particle boundaries and extensive flake-/granule-like by-products surrounding the particles, indicative of intensified interfacial side reactions and the development of a porous, non-uniform CEI. In sharp contrast, $LiCoO_2$ cathodes cycled in the T-electrolyte maintain markedly improved morphological integrity at both 25°C (**Fig. 5**k) and –20°C (**Fig. 5**l). The particles preserve clear outlines with a comparatively compact and conformal surface layer, and no obvious pulverization or severe cracking is observed at the micrometer scale. Even under cryogenic condition, only mild surface texturing is present, consistent with a more stable CEI that mitigates continuous parasitic reactions. These morphological observations align with the XPS analyses, supporting that the T-electrolyte constructs a chemically more stable, inorganic-enriched interphase that better preserves cathode surface integrity.

To further elucidate the interfacial kinetics regulated by different electrolytes, *ex situ* EIS measurements were performed at both 25°C and –20°C. At 25°C, the CE exhibits pronounced and strongly state-of-charge-dependent high-frequency semicircles in the Nyquist plots (**Fig. 5**m). Specifically, the semicircle shrinks progressively during charging from 2.8 to 4.2 V, reaching a minimum resistance at high voltage, and then re-expands during discharge, indicating a clear impedance hysteresis over the charge-discharge trajectory. The statistical summary **(Fig. 5**o) quantifies this

non-monotonic evolution, with the interfacial resistance varying broadly from 180 Ω (C4.2) to ~106 Ω (C2.8), and remaining relatively high at the discharge end (175 Ω at D2.8). The resulting U-shaped SOC dependence indicates that the CE impedance is not solely dictated by instantaneous SOC, but is strongly path-dependent: cathode charge-transfer and transport are intrinsically facilitated at high delithiation, whereas interphase evolution and residual side reactions progressively penalize the interface during the discharge trajectory and at lower potentials. In contrast, batteries employing the T-electrolyte display markedly contracted semicircles at 25°C with much weaker SOC dependence (**Fig. 5**n). The interfacial resistance is consistently reduced to ~63–92 Ω across all states, and the hysteresis between charge and discharge is substantially suppressed. This behavior indicates that the interface layers between electrodes and electrolyte formed in the T-electrolyte is more ionically permeable and chemically self-limiting, thereby stabilizing charge-transfer processes and preventing large SOC-driven impedance excursions. This weaker SOC dependence can be attributed to the cooperative regulation of solvation structure and interphase chemistry. The weakly coordinated Li^+ solvation sheath with moderate anion participation is expected to reduce the desolvation difficulty and make interfacial charge transfer less sensitive to changes in electrode lithiation state. Meanwhile, the compact interphase enriched with LiF, $LiSO_xF$ and borate species limits continuous resistance accumulation and impedance hysteresis during cycling by maintaining stable ion transport pathways across the electrode electrolyte interface. Upon lowering the temperature to –20°C, the impedance response of CE deteriorates markedly (**Fig. 5**p). The Nyquist plots show significantly enlarged semicircles together with pronounced low-frequency diffusion features, suggesting strongly hindered charge transfer and Li^+ transport under cryogenic conditions. Quantitative comparison (**Fig. 5**r) shows that the interfacial resistance of the CE increases dramatically to ~229–251 Ω across the investigated states, consistent with the formation of a thick, organic-carbonate-rich electrolyte interphase that impedes ion transport at low temperature. By contrast, the T-electrolyte maintains relatively compact Nyquist semicircles even at −20°C (Fig. 5q), with interfacial resistance predominantly distributed in the range of ~81–121 Ω (Fig. 5r) and exhibiting much weaker SOC dependence. Overall, the *ex situ* EIS results clearly demonstrate that the

T-electrolyte substantially mitigates interfacial resistance growth and stabilizes interfacial kinetics over a wide temperature window, the results demonstrate that the T-electrolyte mitigates interfacial resistance buildup and stabilizes interfacial kinetics over a wide temperature window. These electrochemical trends are in excellent agreement with the XPS evidence of an inorganic-enriched, LiF-dominated electrolyte interphase and the SEM observations of a compact and conformal interphase, collectively supporting the superior interfacial stability enabled by the T-electrolyte under both ambient and cryogenic conditions.

XRD analysis further provides complementary evidence for the structural stability of $LiCoO_2$ cathodes under the two electrolyte systems. The pristine electrode exhibits sharp, well-resolved reflections characteristic of layered $LiCoO_2$ (Fig. S17), confirming the intact crystalline framework before cycling. After cycling in the CE, these $LiCoO_2$ reflections become significantly attenuated, suggesting substantial structural/phase degradation and/or reduced diffracting volume due to cathode surface reconstruction and accumulated interphase by-products. Meanwhile, LiF reflections remain weak, implying limited formation of crystalline LiF-containing inorganic components on the cathode (Fig. S18).[47] By contrast, cathodes cycled in the T-electrolyte retain much stronger $LiCoO_2$ diffraction intensities together with clearly enhanced LiF-related reflections (Fig. S19), consistent with improved cathode structural preservation and enhanced inorganic (LiF-rich) interphase formation during low temperature cycling. Low-temperature electrolyte design requires not only high ionic conductivity and low viscosity, but also optimized ion speciation, weakened Li^+ solvation and stable anion-derived SEI/CEI formation. The present T-electrolyte follows this principle by coupling viscosity regulation, anion participating solvation and inorganic rich interphase construction, while using iBA to weaken PC dominated Li^+ coordination and preserve low temperature fluidity.

Conclusion

In summary, a wide-temperature tri-salt electrolyte system integrates $LiBF_4$, LiFSI, and LiDFOB in a PC/DME/iBA solvent matrix has been successfully developed for batteries. By jointly tuning salt dissociation, anion-participating solvation, and solvent coordination strength, the optimized electrolyte enables fast Li^+ transport from –20 to 40 °C and stabilizes both anode SEI and cathode CEI chemistries across the temperature window. Raman spectroscopy and MD simulations collectively confirm that the T-electrolyte reconstructs the Li^+ solvation sheath by attenuating PC carbonyl coordination and introducing persistent iBA participation together with competitive FSI^-/$DFOB^-$ contacts, yielding a weaker and more temperature-resilient solvation environment. Coordination-number and cluster-energy analyses further show a marked reduction of PC coordination (from ~24.7% in CE to ~11.8% in T) and lower representative binding energies (5.41–5.83 vs 6.09–9.23 eV), providing a molecular basis for reduced desolvation barriers, faster Li^+ transport, and anion-derived inorganic-enriched interphases under subzero operation. As a result, Li||$LiCoO_2$ batteries exhibit high reversibility, strong rate capability, and durable cycling at subzero temperature, retaining ~85.5% of the room-temperature capacity after 500 cycles at –20°C (0.2 C), Whereas the reference electrolyte-based batteries retain merely 52.1% of the room-temperature capacity after 500 cycles at –20°C (0.2 C), suffering rapid performance degradation under the same conditions. These findings underscore that synergistic regulation of solvation chemistry and interphase formation is a practical design principle for achieving long-lived, low-temperature Li-storage capability, and that further performance improvement may be achieved by balancing salt dissociation, viscosity, effective Li^+ mobility and anion-derived interphase robustness.

Acknowledgements

This work was financially supported by the National Key R&D Program of China (2024YFE0108500), Jiangsu Province Qinglan Project.

Conflict of Interest

The authors declare no competing financial interest.

References

[1] He Y, Chen W, (2025) Analysis of electrochemical performances in hybrid lithium-ion/lithium metal battery during charging. J. Power Sources 654:237835. https://doi.org/10.1016/j.jpowsour.2025.237835

[2] Zhang Y, Lu Y, Jin J, et al (2024) Electrolyte design for lithium-ion batteries for extreme temperature applications. Adv Mater 36:2308484. https://doi.org/10.1002/adma.202308484

[3] He X, Ling Y, Wu Y, et al (2025) Research progress of electrolytes and electrodes for lithium- and sodium-ion batteries at extreme temperatures. Small 21:2412817. https://doi.org/10.1002/smll.202412817

[4] Khan MS, Shahali H, Amiri A (2025) Modeling, analysis of solvation structure, and interfacial reaction dynamics in advanced low-temperature lithium-ion batteries. Energy Storage Mater 80:104363. https://doi.org/10.1016/j.ensm.2025.104363

[5] Shen X, Yang Y, Zhang X, Chen M (2023) Modeling and simulation in rate performance of solid-state lithium-ion batteries at low temperatures. J Energy Storage 74:109296. https://doi.org/10.1016/j.est.2023.109296

[6] Holoubek J, Liu H, Wu Z, et al (2021) Tailoring electrolyte solvation for Li metal batteries cycled at ultra-low temperature. Nat Energy 6:303–313. https://doi.org/10.1038/s41560-021-00783-z

[7] Fan X, Ji X, Chen L, et al (2019) All-temperature batteries enabled by fluorinated electrolytes with non-polar solvents. Nat Energy 4:882–890. https://doi.org/10.1038/s41560-019-0474-3

[8] Ou J, Senevirathna I, Tatagari V, et al (2025) Boosting the ionic conductivity of amorphous oxychloride solid electrolytes via different degrees of amorphization. Energy Mater 5:1–14. https://doi.org/10.20517/energymater.2024.277

[9] Yoon E, Lee J, Byun S, et al (2022) Passivation failure of Al current coll

ector in $LiPF_6$ -based electrolytes for lithium-ion batteries. Adv Funct Mate r 32:2200026. https://doi.org/10.1002/adfm.202200026

[10] Song G, Yi Z, Su F, et al (2023) Boosting the low-temperature performan ce for Li-ion batteries in $LiPF_6$ -based local high-concentration electrolyte. ACS Energy Lett 8:1336–1343. https://doi.org/10.1021/acsenergylett.2c02903

[11] Yuan S, Cao S, Chen X, et al (2024) Deshielding anions enable solvation chemistry control of $LiPF_6$ -based electrolyte toward low-temperature lithiu m-ion batteries. Adv Mater 36:2311327. https://doi.org/10.1002/adma.202311 327

[12] Lee H, An H, Chang H, et al (2023) Boosting interfacial kinetics in extre mely fast rechargeable Li-ion batteries with linear carbonate-based, LiPF6-c oncentrated electrolyte. Energy Storage Mater 63:102995. https://doi.org/10.1 016/j.ensm.2023.102995

[13] Yi T-F, Wei T-T, Li Y, et al (2020) Efforts on enhancing the Li-ion diffusi on coefficient and electronic conductivity of titanate-based anode materials for advanced Li-ion batteries. Energy Storage Mater 26:165–197. https://doi. org/10.1016/j.ensm.2019.12.042

[14] Yu Y, Zhu J, Zhang J, Jiang M (2026) Bridging conductivity and stability: challenges and progress in organic ionic-electronic conductors for overcom ing Si anodes degradation in high-energy lithium-ion batteries. Prog Mater Sci 156:101546. https://doi.org/10.1016/j.pmatsci.2025.101546

[15] Thenuwara AC, Shetty PP, McDowell MT (2019) Distinct nanoscale interp hases and morphology of lithium metal electrodes operating at low tempera tures. Nano Lett 19:8664–8672. https://doi.org/10.1021/acs.nanolett.9b03330

[16] Qin M, Liu M, Zeng Z, et al (2022) Rejuvenating propylene carbonate-bas ed electrolyte through nonsolvating interactions for wide-temperature Li-ions batteries. Adv Energy Mater 12:2201801. https://doi.org/10.1002/aenm.2022 01801

[17] Sheng L, Zhu D, Yang K, et al (2024) Unraveling the hydrolysis mechanis m of $LiPF_6$ in electrolyte of lithium ion batteries. Nano Lett 24:533–540. https://doi.org/10.1021/acs.nanolett.3c01682

[18] Chen G, Qiao L, Xu G, et al (2024) A highly-fluorinated lithium borate main salt empowering stable lithium metal batteries. Angew Chem Int Ed 63:e202400797. https://doi.org/10.1002/anie.202400797

[19] Choi N-S, Chen Z, Freunberger SA, et al (2012) Challenges facing lithium batteries and electrical double-layer capacitors. Angew Chem Int Ed 51:9994–10024. https://doi.org/10.1002/anie.201201429

[20] Zhou D, Gao G, Yang Z, et al (2025) A low-cost inorganic oxide as dual-functional electrolyte additive towards long cycling Li-rich Mn-based cathode materials. Energy Mater 5:500033. https://doi.org/10.20517/energymater.2024.186

[21] Li Q, Jiao S, Luo L, et al (2017) Wide-temperature electrolytes for lithium-ion batteries. ACS Appl Mater Interfaces 9:18826–18835. https://doi.org/10.1021/acsami.7b04099

[22] Mandal BK, Padhi AK, Shi Z, et al (2006) New low temperature electrolytes with thermal runaway inhibition for lithium-ion rechargeable batteries. J Power Sources 162:690–695. https://doi.org/10.1016/j.jpowsour.2006.06.053

[23] Elia GA, Nobili F, Tossici R, et al (2015) Nanostructured tin–carbon/ LiNi0.5Mn1.5O4 lithium-ion battery operating at low temperature. J Power Sources 275:227–233. https://doi.org/10.1016/j.jpowsour.2014.10.144

[24] Wei Y, Wang H, Lin X, et al (2025) Moderate solvation structures of lithium ions for high-voltage lithium metal batteries at -40 °C. Energy Environ Sci 18:786–798. https://doi.org/10.1039/D4EE03192J

[25] Wang L, Yu F-D, Que L-F, et al (2024) 12-ah-level Li-ion pouch cells enabling fast charging at temperatures between -20 and 50 °C. Adv Funct Mater 34:2408422. https://doi.org/10.1002/adfm.202408422

[26] Qin N, Chen J, Lu Y, et al (2024) Trace $LiBF_4$ enabling robust LiF-rich interphase for durable low-temperature lithium-ion pouch cells. ACS Energy Lett 9:4843–4851. https://doi.org/10.1021/acsenergylett.4c01616

[27] Jin F, Ellingsen IS, Fadillah L, et al (2025) $LiBF_4$-derived coating on $LiCoO_2$ for 4.5 V operation of Li_6PS_5Cl-based solid-state batteries. Energy Environ. Mater 8:e70047. https://doi.org/10.1002/eem2.70047

[28] Liu Y-K, Zhao C-Z, Du J, et al (2023) Research progresses of liquid electrolytes in lithium-ion batteries. Small 19:2205315. https://doi.org/10.1002/smll.202205315

[29] Zhao Y, Hu Z, Zhao Z, et al (2023) Strong solvent and dual lithium salts enable fast-charging lithium-ion batteries operating from -78 to 60 °C. J Am Chem Soc 145:22184–22193. https://doi.org/10.1021/jacs.3c08313

[30] Xue W, Qin T, Li Q, et al (2022) Exploiting the synergistic effects of multiple components with a uniform design method for developing low-temperature electrolytes. Energy Storage Mater 50:598–605. https://doi.org/10.1016/j.ensm.2022.06.003

[31] Chang Z, Qiao Y, Yang H, et al (2020) Beyond the concentrated electrolyte: further depleting solvent molecules within a li^+ solvation sheath to stabilize high-energy-density lithium metal batteries. Energy Environ Sci 13:4122–4131. https://doi.org/10.1039/D0EE02769C

[32] Su H, Liu P, Liu Y, et al (2023) Fine-tuning Li+ solvation structure enabled by steric effect and solvating chemistry of the anion for practical electrolyte engineering. Nano Energy 115:108722. https://doi.org/10.1016/j.nanoen.2023.108722

[33] Ma T, Ni Y, Wang Q, et al (2022) Optimize lithium deposition at low temperature by weakly solvating power solvent. Angew Chem Int Ed 61:e202207927. https://doi.org/10.1002/anie.202207927

[34] Huang Y, Fang H, Geng J, et al (2024) Anionic solvation transition at low temperatures for reversible anodes in lithium–oxygen batteries. J Am Chem Soc 146:26516–26524. https://doi.org/10.1021/jacs.4c10187

[35] Qu Z, Xue P, Hu X, et al (2025) Strongly and weakly solvating solvents Co-coordinated electrolyte for stable lithium metal batteries. ACS Energy Lett 10:2913–2923. https://doi.org/10.1021/acsenergylett.5c01025

[36] Wang Z, Li S, Zheng Y, et al (2025) Pre-constructed mechano-electrochemical adaptive solid electrolyte interphase to enhance li^+ diffusion kinetics and interface stability for chemically prelithiated SiO anodes. Adv Sci 12:e15555. https://doi.org/10.1002/advs.202515555

[37] Fang Z, Yang Y, Zheng T, et al (2021) An all-climate CFx/Li battery with mechanism-guided electrolyte. Energy Storage Mater 42:477–483. https://doi.org/10.1016/j.ensm.2021.08.002

[38] Lv W, Zhu C, Chen J, et al (2021) High performance of low-temperature electrolyte for lithium-ion batteries using mixed additives. Chem Eng J 418:129400. https://doi.org/10.1016/j.cej.2021.129400

[39] Zhang SS, Xu K, Jow TR (2004) Electrochemical impedance study on the low temperature of Li-ion batteries. Electrochim Acta 49:1057–1061. https://doi.org/10.1016/j.electacta.2003.10.016

[40] Parimalam BS, Lucht BL (2018) Reduction reactions of electrolyte salts for lithium ion batteries: $LiPF_6$, $LiBF_4$, LiDFOB, LiBOB, and LiTFSI. J Electrochem Soc 165:A251–A255. https://doi.org/10.1149/2.0901802jes

[41] Wang Q, Yao Z, Zhao C, et al (2020) Interface chemistry of an amide electrolyte for highly reversible lithium metal batteries. Nat Commun 11:4188. https://doi.org/10.1038/s41467-020-17976-x

[42] Ding J-F, Xu R, Ma X-X, et al (2022) Quantification of the dynamic interface evolution in high-efficiency working Li-metal batteries. Angew Chem Int Ed 61:e202115602. https://doi.org/10.1002/anie.202115602

[43] Peng Y, Ding M, Zhang K, et al (2024) Quantitative analysis of the coupled mechanisms of lithium plating, SEI growth, and electrolyte decomposition in fast charging battery. ACS Energy Lett 9:6022–6028. https://doi.org/10.1021/acsenergylett.4c02898

[44] Li Y-S, Ye Y-L, Xie Z-X, et al (2025) Mechanically adaptive cathode–electrolyte interphase via dynamic covalent chemistry for long-life Ni-rich lithium batteries. J Am Chem Soc 147:36244–36253. https://doi.org/10.1021/jacs.5c09355

[45] Chen T-L, Liu M, Fan X-Y, et al (2024) Nonflammable sulfone-based electrolytes with mechanically and thermally stable interfaces enabling $LiNi_{0.5}Mn_{1.5}O_4$ to operate at high temperature. ACS Energy Lett 9:5452–5460. https://doi.org/10.1021/acsenergylett.4c02458

[46] Liu X, Fu A, Lin J, et al (2023) Constructing a stabilized cathode electrolyte interphase for high-voltage $LiCoO_2$ batteries via the phenylmaleic anhydride additive. ACS Appl Energy Mater 6:2001–2009. https://doi.org/10.1021/acsaem.2c03934

[47] He X, Zhang Y, Li H, et al (2025) Dual-descriptor tailoring: rational solvent molecule tuning enables high-voltage Li-ion batteries. Adv Mater 37:2417076. https://doi.org/10.1002/adma.202417076